

# Impact of lens distortions on strain measurements obtained with 2D digital image correlation

P. Lava <sup>a,\*</sup> , W. Van Paepegem <sup>b</sup> , S. Coppieters <sup>a</sup> , I. De Baere <sup>b</sup>  
, Y. Wang <sup>c</sup> and D. Debruyne <sup>a,c</sup>

<sup>a</sup>*Catholic University College Ghent, Association K.U. Leuven, Department of Mechanical Engineering, Gebroeders De Smetstraat 1, B-9000 Gent, Belgium*

<sup>b</sup>*Department of Materials Science and Engineering, Ghent University, Technologiepark 903, 9052 Zwijnaarde (Gent), Belgium*

<sup>c</sup>*Department MTM, Katholieke Universiteit Leuven, Kasteelpark Arenberg 44, B-3001 Leuven (Heverlee), Belgium*

---

## Abstract

The determination of strain fields based on displacements obtained via digital image correlation (DIC) at the micro-strain level (  $\leq 1000 \mu m/m$  ) is still a cumbersome task. In particular when high-strain gradients are involved, e.g. in composite materials with multidirectional fibre reinforcement, uncertainties in the experimental setup and errors in the derivation of the displacement fields can substantially hamper the strain identification process. In this contribution, the aim is to investigate the impact of lens distortions on strain measurements. To this purpose, we first perform pure rigid body motion experiments, revealing the importance of precise correction of lens distortions. Next, a uni-axial tensile test on a textile composite with spatially varying high strain gradients is performed, resulting in very accurately determined strains along the fibers of the material.

*Key words:* Digital image correlation, lens distortions, high strain gradients, composite materials

---

---

\* Corresponding author. Tel.: +32 9 267 27 06; fax: +32 9 2658648  
E-mail address: pascal.lava@kahosl.be (P. Lava).

## 1 Introduction

Optical full-field measurement methods such as Digital Image Correlation (DIC) are currently extensively applied to study the deformation characteristics of a wide range of materials [1–6]. Moreover, the understanding of the complex structural deformation behavior of fibre reinforced composites is often based on local strain analysis [7,8]. The measured strain fields, however, are concentrated at the micro-strain level (  $\leq 1000 \mu m/m$  ) resulting in high uncertainties due to the experimental setup and errors in the derivation of the displacement fields. Notwithstanding, an excellent control on the accuracy and precision of the obtained displacement and strain results is a clear prerequisite before one can embark on e.g. the validation of numerical simulations or the identification of material parameters via inverse methodology.

In the past, various numerical studies have been performed to validate the accuracy of DIC displacement and strain fields [9–13]. The impact of out-of-plane motion on 2D and 3D digital image correlation measurements has been intensively investigated in Ref.[14], whereas the influence of lens distortions on the measured displacement fields was studied in Ref.[15]. How lens distortions affect upon strain fields in microscopic applications was studied in Refs.[16,17]. Few attention, however, has been paid to the impact of lens distortions on the determined strain fields in macroscopic tensile experiments, which will be the subject of this contribution.

Experiments performed in view of material characterization are often in-plane and accordingly involve a single camera setup (2D-DIC). This has several advantages compared to a stereo camera setup, as e.g. (a) reduction in costs (only one camera/microscope involved) and (b) more precise (no cross-camera matching and triangulation). A clear disadvantage, however, is the perpendicularity requirement making the experimental setup more cumbersome. Since no triangulation procedures are involved in 2D measurements, the camera calibration setup is often omitted and with this also the correction for lens distortions in the 2D matching process. A stereo camera setup, on the other hand, urges the input of camera parameters in order to reconstruct the shapes involved. As such, corrections for lens distortion are naturally involved.

One could argue that the influence of lens distortion can be neglected by using an appropriate combination of a CCD camera and lens. This is, however, not always possible or a distortion-free system is too expensive. Moreover, modern lens systems are subject to distortions down to a very small level. As such, one can expect that the impact of distortions at large deformations inducing plastic strains is negligible. We focus on brittle materials, however, with strain fields concentrating at the micro-strain level. For small deformation cases the relative motions between the same points in the reference and deformed images

are also very small, and accordingly one could expect that the relative image aberration between adjacent points due to lens distortions can be ignored. In this contribution it is shown that for micro-strain applications the influence of even small distortion defects can be substantial.

In this contribution, we will undistort the determined displacement fields in single camera experiments via our inhouse DIC system MatchID [18]. In order to study the impact of this distortion correction, we first perform pure rigid body motion experiments. Various lenses of different distortion magnitude are investigated. Next, a uni-axial tensile test on a textile composite with spatially varying high strain gradients and localizations is performed.

Summarizing, it is the purpose of this article to convince the experimentalist that the determination of highly accurate high-strain gradients in macroscopic 2D DIC experiments necessitates the precedence of the test with a scrutinized calibration in order to be able to precisely correct for lens distortions that could result in artificial strain fields.

The outline of this article is as follows. In Sec. 2 we present the formalism for lens distortion determination and corrections. Our results are included in Sec. 3-4. We conclude in Sec. 5.

## 2 Formalism

In this section we briefly outline the procedure that is implemented to account for lens distortions in our correlation algorithms. In addition, we summarize how the distortion parameters for a specific setup are obtained. First, however, some fundamentals on single camera and stereovision DIC are outlined in addition to some details on how the strain fields are calculated from the measured displacements.

### 2.1 *Single camera and stereo vision DIC*

The measurement of displacement fields in single camera and stereovision DIC proceeds as depicted in Fig.1. Basically, a 2D-DIC measurement proceeds as follows. In a subset-based method, also denoted as the local approach, a matching between two speckle patterns - captured at the undeformed and deformed state of the specimen - is accomplished by considering a pixel  $(x_0, y_0)$  and its neighborhood in the undeformed image and searching the same subset in the deformed image, adopting a maximization routine for a similarity function. Allowing the subset to deform according to a specified transformation func-

tion, an optimization routine yields displacement components  $(u_0, v_0)$  with subpixel accuracy.

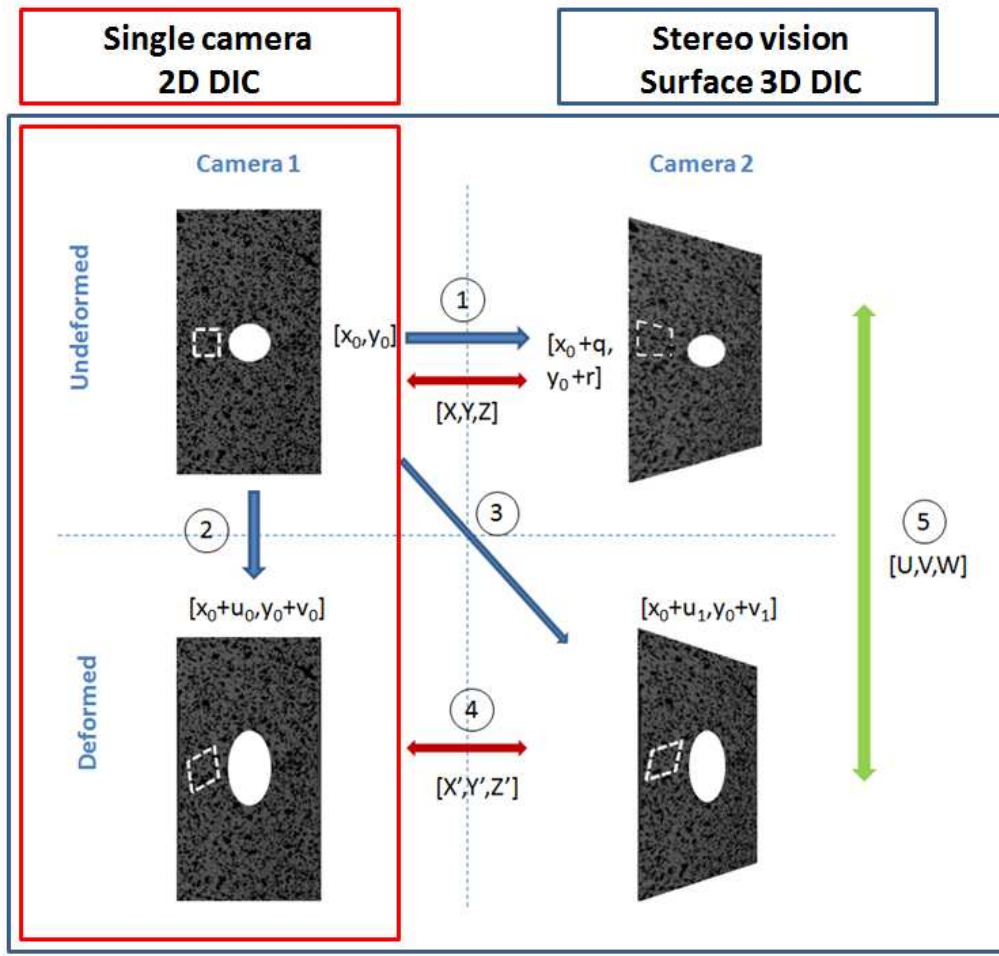


Fig. 1. Schematic view of the process of single camera and stereovision DIC.

Stereo-vision DIC involves a fundamental extension of 2D-DIC correlation concepts with stereovision principles. Indeed, after synchronization of the image acquisition two cameras capture  $M$  pairs of images simultaneously during the experiment. Next, the measurement of 3D surface displacements proceeds as outlined below:

- (1) A subset at  $(x_0, y_0)$  is selected in the reference image of camera 1. Next, 2D-DIC cross-camera correlation yields a displacement vector  $(q, r)$  and matching position in the reference image of camera 2. Thanks to a geometric constraint inherent to any calibrated stereo imaging system, one can reduce this 2D search to a 1D search along the corresponding epipolar line, simplifying the search routine and saving processing time. This process is repeated for a dense map of subsets in the reference image. The determined set of corresponding points and the input of stereo camera parameters results in the initial object shape with 3D coordinates  $(X, Y, Z)$

via a classical triangulation method [19], a process usually referred to as reconstruction.

- (2) The same set of subsets in the reference image of camera 1 is used to perform a standard 2D-DIC correlation to locate the matching positions  $(x_0 + u_0, y_0 + v_0)$  in the deformed image of camera 1.
- (3) The same set of subsets in the reference image of camera 1 is used to perform a cross-camera correlation to identify the matching positions  $(x_0 + u_1, y_0 + v_1)$  in the deformed image of camera 2.
- (4) Again, the obtained set of corresponding points for the deformed images and the input of stereo camera parameters results in the deformed 3D configuration  $(X', Y', Z')$ .
- (5) The 3D displacement field  $(U, V, W)$  corresponding to the specific loading step can now be directly obtained by subtracting  $(X', Y', Z')$  and  $(X, Y, Z)$ .

The abovementioned steps 2 – 5 are repeated for each set of deformed images, yielding a complete track of the deformations in three dimensions. We remark that all displacement components  $(u_0, v_0)$ ,  $(q, r)$  and  $(u_1, v_1)$  can be positive or negative according to tension or compression in the indicated direction.

Single camera DIC experiments are most often applied in view of material testing and model validation and are restricted to planar specimens subject to in-plane deformations. In addition, the single recording camera is assumed to be perpendicularly aligned with the specimen's surface. If not, relative out-of-plane motion of the specimen with respect to the imaging system will introduce image-plane displacement gradients, resulting in corrupted displacement and strain field data [14]. On the other hand, 2D-DIC has the advantage that no errors due to cross-camera matching or triangulation are introduced. In principle, no camera parameters are needed. As such, in a single camera setup the calibration stage is often omitted. Further on, it will be shown that the determination of certain camera parameters, however, can play a crucial role in the accurate determination of the involved displacement and strain fields, in particular when deformation modes at the micro-strain level are probed.

Stereo-vision DIC experiments, on the other hand, are most often invoked in view of structural testing and have less stringent restrictions with respect to the geometry or the loading conditions involved. The correlation processes, however, are more complex and can introduce additional errors. Since the triangulation process urges the input of camera parameters, the calibration process elicits the correction for lens distortions in a natural way.

Once the DIC sub-pixel displacement fields are determined according to the abovementioned principles, we can concentrate on the determination of the strain fields since the displacements contain all the information needed to calculate the in-plane normal strain and shear components  $\epsilon_{xx}$ ,  $\epsilon_{yy}$  and  $\epsilon_{xy}$ .

This calculation involves the determination of the so-called deformation gradient matrix  $\mathbf{F}$ , describing the relative spatial position of two neighbouring particles after deformation in terms of their relative material position before deformation. Expressing the deformation gradient matrix in terms of the horizontal (x-direction) and vertical (y-direction) displacement components  $u$  and  $v$  yields

$$\mathbf{F} = \begin{bmatrix} 1 + \frac{\partial u}{\partial x} & \frac{\partial u}{\partial y} & \frac{\partial u}{\partial z} \\ \frac{\partial v}{\partial x} & 1 + \frac{\partial v}{\partial y} & \frac{\partial v}{\partial z} \\ \frac{\partial w}{\partial x} & \frac{\partial w}{\partial y} & 1 + \frac{\partial w}{\partial z} \end{bmatrix} \quad (1)$$

The determination of the strain tensor in e.g. the logarithmic Euler-Almansi convention  $\epsilon^{\ln EA}$  is now straightforward:

$$\epsilon^{\ln EA} = \ln(\mathbf{V}) = \ln(\sqrt{\mathbf{F}\mathbf{F}^T}) , \quad (2)$$

with  $\mathbf{V}$  the so-called left stretch tensor obtained via the Cauchy theorem of polar decomposition. One motivation to use this strain tensor in the case of metal plasticity is the following: when the true stress is plotted against the logarithmic strain, tension, compression and torsion results nearly coincide [20].

As explained in Ref.[9], in order to improve the strain calculation with increased accuracy, one often initially smooths the estimated displacement fields before starting the differentiation process by finding an analytical expression of a surface, which, in a least squares sense, approximates the experimental displacement field in a selected region. This is a so-called strain window containing  $N \times N$  nearest neighbors for each component of displacement. It is important to remark that the pixel dimensions of this strain window also depend on the step size chosen in the correlation algorithm. Indeed, if e.g. a step size of 5 pixels is used an experimental displacement value is only available every 5 pixels in both horizontal and vertical direction. Accordingly, a  $N \times N$  strain window results in a smoothing area with actual pixel width and height of

$$[(N - 1) \times \text{step size}] + 1 . \quad (3)$$

It speaks for itself, that in particular for regions with high strain gradients the physical dimensions of the strain window must be chosen with care, aiming at a good compromise between noise reduction and the evasion of oversmoothing.

## 2.2 Lens distortions

Lens distortions have several mathematical forms, depending upon the type being modeled. In this contribution we will only consider radial and tangential (or decentering) distortions that occur in imaging systems. There are many other kinds of distortions (amongst these, we recognize spherical, coma, astigmatism, curvature of field, linear, ...) but they have typically lesser effects than radial and tangential distortions. In general, an image distortion model is given as a distortion vector  $\mathbf{D}$  from the undistorted image coordinates to the distorted ones:

$$\mathbf{X}^d = \mathbf{X}^u + \mathbf{D}(\mathbf{X}^u, \zeta_i) , \quad (4)$$

with  $\mathbf{X}^d = (x^d, y^d)$  and  $\mathbf{X}^u = (x^u, y^u)$  referring to the distorted and undistorted sensor positions in the pinhole camera model, respectively, and  $\zeta_i (i = 1, \dots, N)$  representing the distortion parameters for the model. Radial distortions arise as a result of imperfections of the curvature of the lens and often noticeably distort the location of pixels near the edges of the imager. Indeed, rays further from the center of the lens are bent more or less than those closer in. Accordingly, the radial distortion vector  $\mathbf{D}_r$  can be characterized by the first three terms of a Taylor series expansion around the image plane center location and reads

$$\mathbf{D}_r(\mathbf{X}^u, \zeta) = \kappa_1 \rho^3 \mathbf{e}_r + \kappa_2 \rho^5 \mathbf{e}_r + \kappa_3 \rho^7 \mathbf{e}_r , \quad (5)$$

with

$$\rho = \sqrt{[(x^u - c_x)^2 + (y^u - c_y)^2]} \quad (6)$$

the radial distance of the point  $(x^u, y^u)$  relative to the image plane center location  $(c_x, c_y)$  and  $\mathbf{e}_r$  the radial unit vector. The coefficients for radial distortion have units  $\text{pixels}^{-2}$ ,  $\text{pixels}^{-4}$  and  $\text{pixels}^{-6}$ , respectively.

Tangential distortions, on the other hand, result from the assembly process of the camera system as a whole, with the lens not being exactly parallel to the imaging plane yielding a displacement between the principal point and the physical center of the camera image plane. Their impact can be minimally characterized by two additional parameters  $p_1$  and  $p_2$  such that

$$\begin{aligned} x^d = & x^u + (x^u - c_x)(\kappa_1 \rho^2 + \kappa_2 \rho^4 + \kappa_3 \rho^6) \\ & + 2p_1(x^u - c_x)(y^u - c_y) \\ & + p_2 [\rho^2 + 2(x^u - c_x)^2] , \end{aligned}$$

$$\begin{aligned}
y^d = & y^u + (y^u - c_y)(\kappa_1 \rho^2 + \kappa_2 \rho^4 + \kappa_3 \rho^6) \\
& + 2p_2(x^u - c_x)(y^u - c_y) \\
& + p_1 \left[ \rho^2 + 2(y^u - c_y)^2 \right] ,
\end{aligned} \tag{7}$$

Accordingly, the parameters needed to correct for lens distortions are conveniently collected in the vector  $\zeta = [c_x, c_y, \kappa_1, \kappa_2, \kappa_3, p_1, p_2] \in \mathbb{R}^7$ .

As can be inferred from Eq.(4), the distortion map relies on the unknown undistorted sensor locations and accordingly can not directly be determined. In this contribution an iterative optimized Levenberg-Marquardt procedure is used to determine the corrected coordinates from the distorted ones. Accordingly, in our DIC routines the corrected displacement components are determined as follows: (1) a standard correlation algorithm determines the corresponding point  $[(x + u)^d, (y + v)^d]$  of a reference point  $[x^d, y^d]$  (2) for both the reference and corresponding point the undistorted pixel positions are determined according to the formalism outlined above (3) an "undistorted" displacement field  $[u^u, v^u]$  is obtained by subtracting the corrected pixel positions of the corresponding point from the reference point. It is important to note that no a priori undistortion of the images is performed. Indeed, this would involve additional interpolations introducing an extra error source in the correlation routines.

### 2.3 Camera calibration

As discussed above, lens distortion corrections urge the input of camera calibration parameters. In our inhouse calibration platform, these are determined via a bundle adjustment technique as outlined in Ref.[21,22], using various images of a translated and rotated planar regular grid pattern. As such, one arrives at the following set of intrinsic and extrinsic parameters:

- $(c_x, c_y)[pixels]$ : image plane center location for each camera
- $(f_x, f_y)[pixels]$ : focal lengths in horizontal and vertical directions for each camera
- $f_s[pixels]$ : accounting for skewing of sensor array
- $\kappa_1, \kappa_2, \kappa_3$ : radial distortion coefficients
- $p_1, p_2$ : tangential distortion coefficients
- $(T_x, T_y, T_z)$ : translation components to transform origin of camera 1 to origin of camera 2
- $(\theta, \phi, \psi)$ : relative orientation of camera 2 with respect to camera 1, representing a rotation around the X-, Y- and Z-axis, respectively.

The full bundle adjustment technique is a two-step approach. First, a linear approximation yields initial estimates for all calibration parameters except



the distortion parameters, which introduce non-linear effects. Next, within a Levenberg-Marquardt optimization routine, the differences between the measured sensor coordinates and the model predictions of these locations are minimized, yielding calibration results for this non-linear camera model while simultaneously determining the shape of the calibration target up to a scale factor [21]. This significantly reduces the requirements on the calibration target. As such, the world coordinates  $(X_W, Y_W, Z_W)$  of the regular grid pattern enter the Jacobian and Hessian matrices in the optimization approach. Finally, 10 intrinsic parameters,  $6M$  extrinsic parameters positioning the camera relative to the grid for  $M$  calibration views and  $3P$  world coordinates for  $P$  target grid points are estimated. Accordingly, the determination of the camera parameters is a numerical cumbersome task with various error sources. Notwithstanding, an accurate camera parameter determination is of crucial importance in view of precise DIC displacement fields. It is not the purpose of this contribution, however, to perform a scrutinized estimation of errors involved with the calibration process nor to introduce a new calibration procedure. We opted for the full bundle adjustment technique since it is generally adopted in stereovision DIC and as such a direct comparison between 2D DIC and stereovision DIC can be made further on.

In order to validate the accuracy of our inhouse developed calibration routines, further on a comparison to the results obtained with the methods of Tsai [23] and Zhang [24] will be made. In the Tsai method, which has become very popular in the computer vision community, the internal and external parameters are decoupled by decomposing the camera model into linear and nonlinear components. Zhang’s algorithm, on the other hand, retrieves the internal and external parameters by estimating the homography between a model plane containing the calibration target and several images of this target. The Zhang method constitutes the basis of the calibration routines available in the open source platform OpenCV. For a more detailed discussion on these methods we refer the reader to Refs.[25–28]. We stress that all results presented further on receive identical pairs of world coordinates and sensor locations. Accordingly, an objective comparison of the calibration methods is made, not being contaminated by artifacts in the sensor position locations determination.

### 3 Rigid body experiments

The goal of this research is to study the impact of lens distortion corrections on strain field measurements and in particular to improve the accuracy of DIC strain measurements on fibre reinforced composites. Before imposing loading conditions on specimens composed of these materials, we first subject them to pure translational and rotational motion. Deviations from zero can give an indication of the errors on the strain fields at the micro-strain level. We stress,

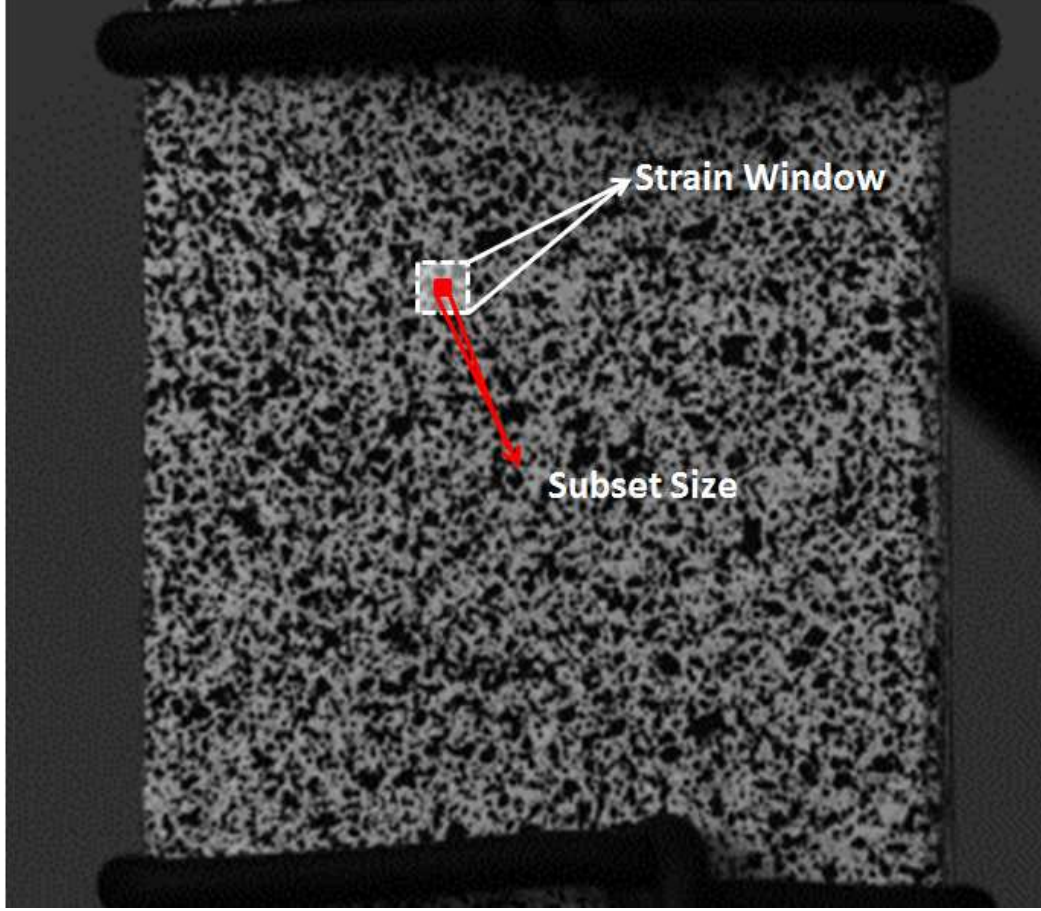


Fig. 2. Speckle pattern used in the rigid body experiments. The red square represents a subset of  $25 \times 25$  pixels<sup>2</sup>, whereas the white square shows a strain window area of  $11 \times 11$  displacement data points.

however, that when larger plastic deformations are involved more complicated (numerical) experiments should be performed in order to quantify the errors of the large plastic strains [10]. The composite materials in this contribution, however, are very brittle with strain values concentrated at the micro-strain level justifying the use of the rigid body approach. In Fig.2 the random speckle pattern is displayed. This was created by first spraying a matte white surface layer on the composite material to avoid reflection. Next, a speckle coat is attached via black paint spraying.

Fig.3 shows the measured artificial strains due to a 1 mm rigid body translation. The experiment is performed with a stereo camera setup with one camera perpendicular to the specimen plane. Both cameras are 8-bit AVT STINGRAY F-201 B 1/1.8" ones with a resolution of  $1624 \times 1232$  pixels<sup>2</sup>. Accordingly, we can mutually compare the results of 2D DIC and stereovision DIC. Both cameras are equipped with a Schneider-Kreuznach Cinegon 12mm 1.4 lens. A calibration procedure as described in Sec.2 results in intrinsic camera parameters that are summarized in columns one and two of table 1 for the

Parameter	12 mm [ $\perp$ ]	12 mm [ $\angle$ ]	23 mm	50 mm [Full]	50 mm [W/O]
$c_x$ (pixels)	797.08	791.66	756.26	784.17	838.32
$c_y$ (pixels)	642.02	620.41	594.25	516.16	533.2
$f_x$ (pixels)	3039.39	2932.52	5294.07	13129.81	13068.17
$f_y$ (pixels)	3075.72	2961.06	5308.75	13125.79	12943.14
$\kappa_1$ ( $\times 10^{-8}$ )	-2.81	-2.41	-0.14	-0.19	-0.22
$\kappa_2$ ( $\times 10^{-15}$ )	-23.42	0.65	-11.11	1.06	-0.35
$\kappa_3$ ( $\times 10^{-21}$ )	17.80	-1.07	-6.90	-0.0062	-0.0021
$p_1$ ( $\times 10^{-7}$ )	-6.58	-8.03	-7.55	2.18	2.3
$p_2$ ( $\times 10^{-7}$ )	-2.76	2.86	-9.80	-6.48	-7.11

Table 1

Calibration parameters for the various lens setups. The first and second column represent the results of a perpendicular and non-perpendicular camera equipped with a a Schneider-Kreuznach Cinegon 12mm 1.4 lens. Column three corresponds to a Schneider-Kreuznach Xenoplan 23 mm 1.4 lens whereas columns four and five refer to a Nikon 50 mm 1.4 lens in a full bundle and full bundle without world coordinates optimization, respectively.

perpendicular and angled camera, respectively. This yields pixel dimensions of 0.02 mm. In order to assess the impact of lens distortions for both maximum and minimum principal strain, a statistic binning procedure is adopted. The full strain range of the measured field is divided into several equidistant intervals, or bins. The mid-point of each interval is considered as the position of the bin and the number of points within the bin constitute the population. As can be inferred, for both 2D and 3D DIC measurements the impact of the inclusion of lens distortion corrections for these specific lenses is substantial, improving the accuracy of DIC on the strain determination down to the 500 micro-strain level.

All results presented are obtained with the following standard DIC implementations [9,10]: subset size  $25 \times 25$  pixels<sup>2</sup>, step size 5 pixels, strain window  $11 \times 11$  displacement data points, bicubic interpolation and an affine transformation order. The subset and strain-window sizes are reflected in Fig.2 in order to have an idea about the magnitude of these values as a function of the resolution and speckle pattern. The size of the strain-window is motivated by the configuration of the fibre reinforced composite on which the test is performed and will be more profoundly motivated further on. Obviously, a larger strain window would improve on the strain accuracy and precision to a great extent. This is, however, not an option since a tensile test on a fibre reinforced material will result in high strain gradients at the micro-strain level and a too large strain window would not be able to capture these strain localizations since too much smoothing is involved.

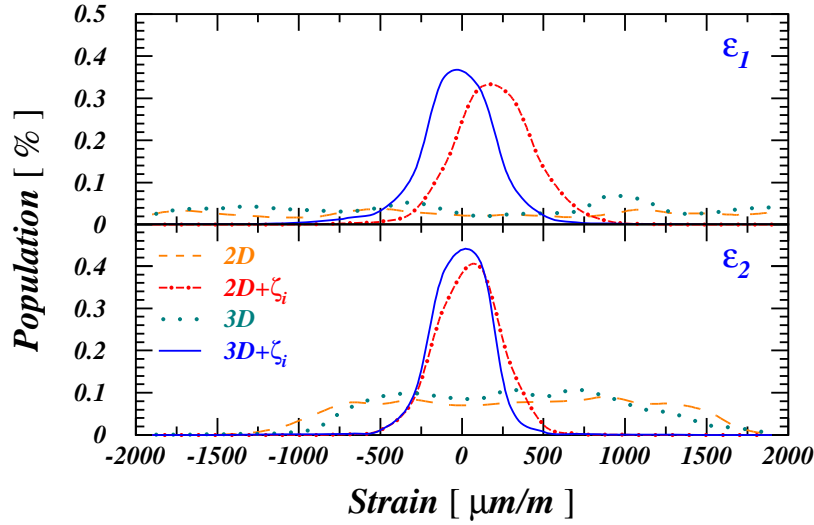


Fig. 3. Impact of lens distortion corrections on the strain errors involved in a 1 mm translation experiment with a Schneider-Kreuznach Cinegon 12mm 1.4 lens. Results show the population as a function of measured strain for both maximum and minimum principal strain fields. The dashed and dotted lines correspond to uncorrected single and stereo camera results, respectively, whereas the dot-dashed and full lines reflect the impact of lens distortion corrections.

It is important to note that this involves a very basic setup in a standard laboratory environment, with no specific attention towards lighting conditions and vibrations. An optimum control of these would improve on the accuracy and precision of these experiments, but the primary focus of this research is on the impact of lens distortions on the determined strain fields. The slight shift between the 2D and 3D results is due to small defects in the perpendicular alignment of the camera. This is in accordance with the results of Ref.[14], stressing the importance of out-of-plane motion deformations in single camera experiments. Accordingly, in a 2D experiment it is of the utmost importance to fulfill the experimental conditions to a great extent.

Next, attention is paid to a 2 degree in-plane rotational experiment. As for the pure rigid translational experiments, ideally zero strain fields should be retrieved. In Fig.4 the population distribution as a function of measured strains is displayed. In this experiment only a single camera setup is considered equipped with a Schneider-Kreuznach Xenoplan 23 mm 1.4 lens yielding intrinsic camera parameters as summarized in the third column of table 1 and resulting in pixel dimensions of 0.08 mm. As can be inferred, similar conclusions can be drawn as for the translational experiment and the 12 mm lens, stressing the impact of lens distortions. Correcting for these improves the accuracy down to the 300 micro-strain level.

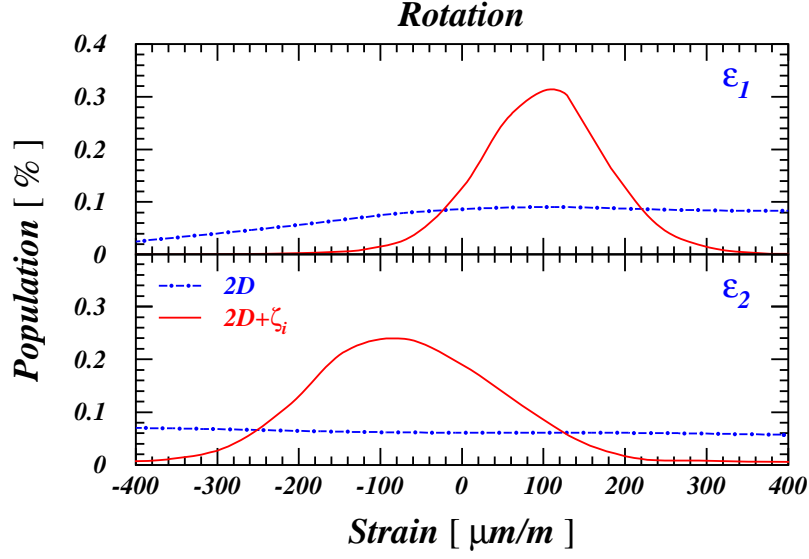


Fig. 4. Impact of lens distortion corrections on the strain errors involved in a 2 degree rotation experiment with a Schneider-Kreuznach Xenoplan 23 mm 1.4 lens. Results show the population as a function of measured strain for both maximum and minimum principal strain fields. The dot-dashed (full) line show the results of a single camera measurement with (without) lens distortion corrections.

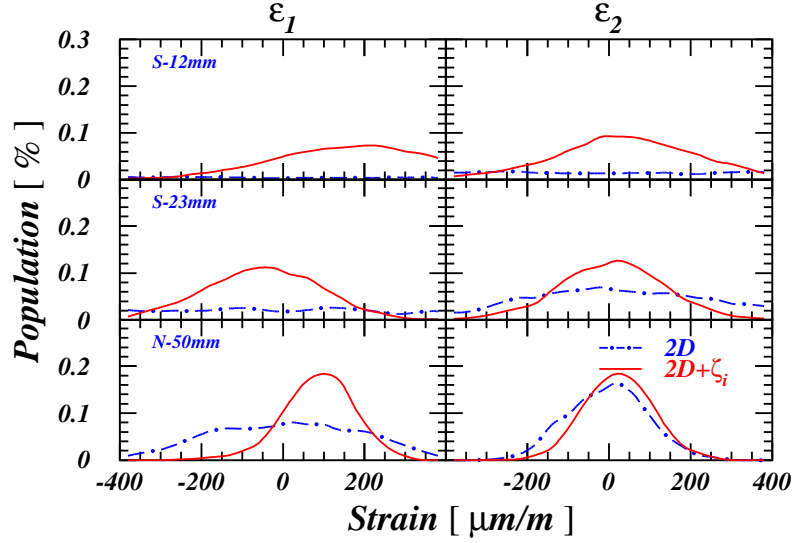


Fig. 5. Impact of lens distortions on the strain errors in a single camera 10 mm translation experiment for various lens configurations.

In order to investigate the consistency of the impact of lens distortions for various lens configurations, a single perpendicular camera 10 mm translational experiment is performed for a camera equipped with three different lens types: a

Schneider-Kreuznach Xenoplan 12 mm 1.4 lens, a Schneider-Kreuznach Xenoplan 23 mm 1.4 lens and a Nikon 50 mm 1.4 lens. For this last setup, an additional lens spacer of 15 mm was used in order to improve on the spatial resolution of the specimen. Finally, pixel dimensions of 0.017 mm are obtained for this setup and the camera calibration parameters in a full bundle approach are displayed in the fourth column of table 1. As can be inferred from Fig. 5, all three configurations show a substantial impact of lens distortions on the final strain field determination, in particular for the maximum principle strain  $\epsilon_1$ . This is not surprising since the displacements are uni-axially applied. The rotational experiment of Fig.4, on the other hand, involves displacements in both horizontal and vertical directions and introduces improvements that are equally large for both principal strains. The highest accuracy for the 10 mm translational experiment is obtained with the Nikon 50 mm lens, where the inclusion of lens distortions improves the accuracy up to 200  $\mu m/m$ . Accordingly, all results presented further on are obtained with a camera equipped with the Nikon 50mm 1.4 lens.

As outlined in Eqs.(5-7) various radial and decentering parameters enter the correction model for lens distortions. In Fig.6 the impact of these on the accuracy of the measured strain fields is investigated in a 1mm translation experiment. As can be inferred, bulk of the corrections is due to the introduction of the first order radial distortion parameter. The impact of higher order radial distortions is marginal and accordingly can be safely neglected. The first decentering parameter  $p_1$  invokes a slight shift of the Gaussian peak in both the minimum and maximum principal strain, whereas the effect of  $p_2$  is negligible. Accordingly, we can conclude that it is in particular the first order radial distortion coefficient  $\kappa_1$  that can improve on the strain accuracy to a great extent. Again, the impact on the minimum principal strain  $\epsilon_2$  is smaller due to the uni-axial character of the displacements introduced.

In order to validate the results of our inhouse developed calibration platform and its impact on the accuracy of strain field determination, a comparison to other available calibration platforms is made as outlined in Sec. 3. The results of these are summarized in Fig.7 for the identical 1 mm translation experiment of Fig.6. Once more we stress that all these routines are integrated into one software platform, all receiving the same pairs of world coordinates and sensor locations. As can be inferred, our implemented full bundle approach agrees very well to the results of the Zhang algorithm. In addition, we estimate the impact of omitting the optimization of the world coordinate locations  $(X_W, Y_W, Z_W)$  in the bundle approach. This could lead to a more stable optimization routine since less parameters to optimize are involved. The camera parameters obtained in this bundle approach without optimizing the world coordinate positions are listed in the last column of table 1. It is clear that the effect of this omission is marginal on the final strain accuracy. We remark, however, that in stereovision DIC the optimization of the world coordinates

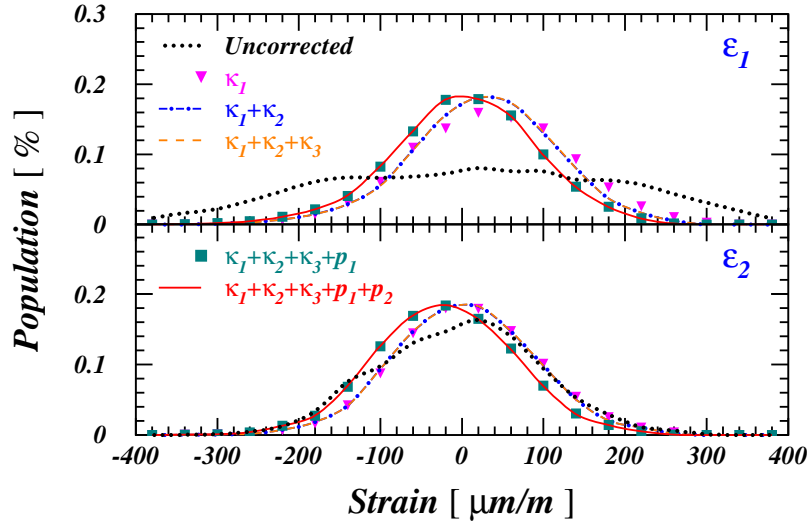


Fig. 6. Impact of various lens distortion parameters on the minimum and maximum principal strain errors in a single camera 1 mm translation experiment. The dotted line shows the results without corrections for lens distortions. The triangles, dot-dashed and dashed lines correspond to the introduction of first, second and third order radial distortions. The squares and the full line take additionally into account the first and second decentering parameter, respectively.

can play an important role in the accuracy of the shape reconstruction. Next to the default Zhang approach, one can run this routine without the inclusion of the decentering parameters. It is shown in Fig.7 that the impact of this omission in the Zhang approach is substantial, not only introducing a shift as was the case for the full bundle in Fig.6, but also unfolding the Gaussian distribution. Finally, the Tsai results also show a lower strain accuracy, of the same order as the Zhang approach omitting the tangential components.

To conclude, we can state that our inhouse implemented full bundle adjustment calibration approach adequately corrects for distortion effects obtaining strain fields with an accuracy down to  $200 \mu\text{m}/\text{m}$ . These predictions are in line with the results obtained with standard available calibration platforms.

#### 4 Uni-axial tensile test

Now that we are confident about the accuracy of the strain fields at the micro-strain level, we can embark on a real uni-axial tensile test on a fibre reinforced composite. The selected material is a five-harness satin weave carbon/Polyphenylene Sulphide (PPS) thermoplastic composite used extensively

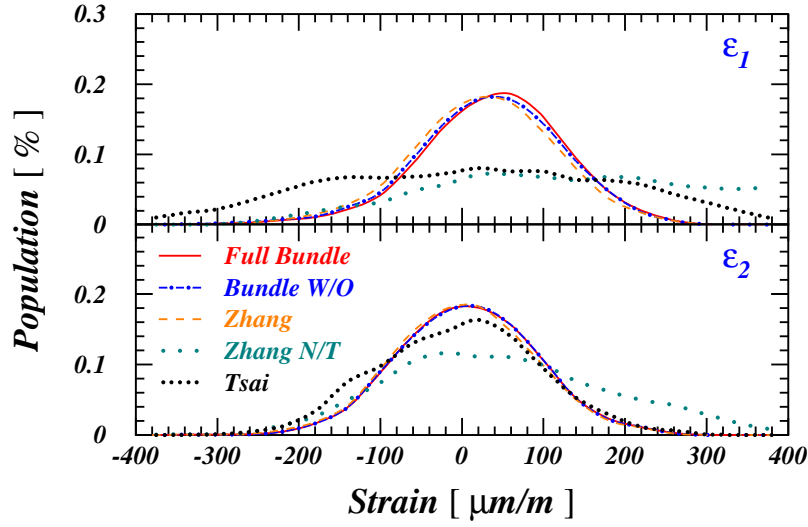


Fig. 7. Impact of calibration algorithm on the strain errors in a single camera 1 mm translation experiment. The solid line shows the result of the full bundle adjustment approach, whereas the dot-dashed line corresponds to the full bundle without the optimization of the world coordinates. The dashed, dotted and small-dotted lines represent the default Zhang, the Zhang without tangential distortions and the Tsai model results, respectively.

on the Airbus A380 and A350. In five-harness satin weave, one warp yarn runs over four weft yarns and under one weft yarn. Satin weave is pliable and has the ability to conform to complex and compound contours. Polyphenylene Sulphide (PPS) is a high-end thermoplastic matrix that is used in aerospace applications. The so-called unit cell, repetitive building block of the weaving pattern, is about 7.4 mm by 7.4 mm wide, and is schematically depicted in the left panel of Fig.8. The interlacing pattern of the weft and warp yarns can be clearly distinguished. Important for the later strain analysis, is that the cross-over points (where warp and weft yarns are interlacing) can be found on diagonal lines, relative to the orthogonal warp and weft directions. The top surface of the carbon/PPS specimen looks like the right panel of Fig.8. The black parts are the impregnated carbon/PPS yarns, while the white resin pockets are the semi-crystalline PPS matrix.

#### 4.1 FE simulations

In the numerical simulations, a finite element model of the unit cell of the fabric is developed. The geometry of the weft and warp yarns has been determined from micro-tomography measurements, and the corresponding geometry of the representative volume element of the carbon satin weave/PPS composite



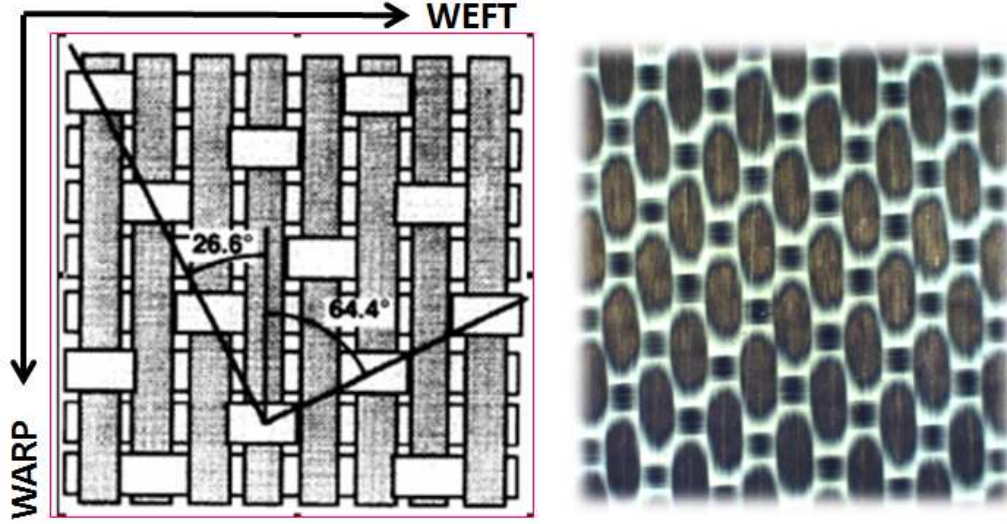


Fig. 8. Unit cell of five-harness satin weave carbon/PPS thermoplastic composite (left panel) and top surface of the specimen (right panel)

has been meshed. The eight carbon/PPS layers in the composite are stacked on top of each other, and in-plane periodic boundary conditions are applied to the mesh, to simulate the in-plane repetitive behaviour of the unit cell stack. Computation of the homogenized elastic properties of this unit cell model showed very good agreement with the experimental data, confirming the validity of this model. More details can be found in Refs. [7,29]. Next, a tensile load is applied in the x-direction, corresponding to the warp direction of the fabric. Under this loading, Fig. 9 shows the local stress  $\sigma_{22}$  in the local coordinate system of the orthotropic yarns (both weft and warp). That means that  $\sigma_{22}$  is for each yarn, the in-plane stress transverse to the direction of the fibre filaments in that yarn. The  $\sigma_{22}$  stress shows the largest value at the cross-over points of the warp and weft yarns, indicating the largest risk of transverse cracking of the weft yarns at those locations [30,31]. The diagonal patterns of the stress concentrations are clearly visible.

#### 4.2 Experiment

When an experimental tensile test is performed, it is indeed confirmed that the transverse cracking occurs in the weft yarns, under a perfect diagonal pattern at the surface of the specimen. The left image in Fig.10 shows a view of the top surface of the specimen. The polishing is not of ideal quality, but it is much more difficult to polish the top surface than the edges. An identical diagonal cracking pattern as obtained via the FE simulations is observed at the cross-over points of the weft yarns with the warp ones. In the right image of Fig.10 a detail of a polished cross-section of the edge of the specimen is shown, close to the top surface (top of the picture). The transverse crack is about in the

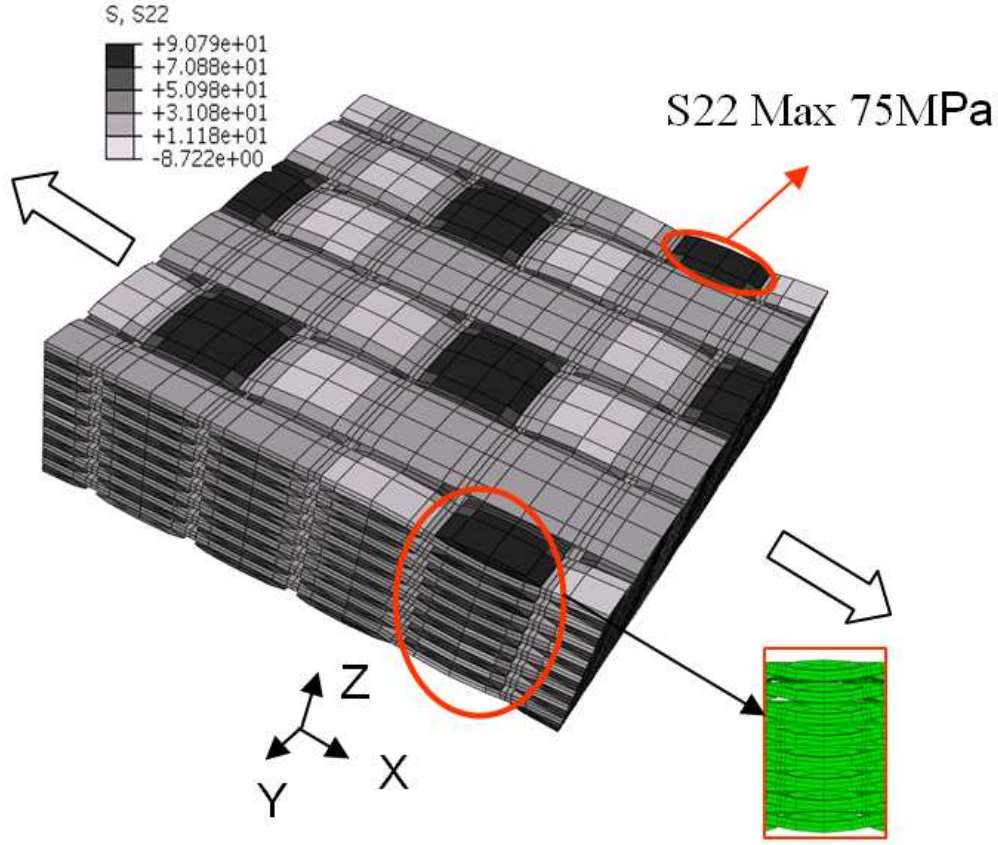


Fig. 9. Finite element model of the unit cell subject to a tensile load in warp direction.

middle of the weft yarn, where it is crossing the warp yarn (underneath it).

In order to measure the displacement and strain fields at the surface of the specimen with digital image correlation the speckle pattern of Fig.2 is attached to the specimen with mat white paint and black speckles. Next, the camera is equipped with a Nikon 50 mm 1.4 lens, yielding calibration parameters with the full bundle approach as listed in table 1. Images are captured at static intervals of 5kN up to 35kN. As outlined above, in particular the strain window dimensions (or smoothing area) in the processing of the images must be chosen with care. Indeed, a too small strain window would reintroduce noise in the derived strain fields [9], whereas too large dimensions would contaminate the strain in e.g. the cross-over points of the warp and weft yarns with neighboring information. As such, the dimensions of the yarns are first measured with micro-CT and result in a yarn width of  $1.31 \pm 0.01$  mm. As outlined above, the experimental setup yields a spatial resolution of 1 pixel equal to 0.017 mm. As such, the strain window influence width and height must not exceed 77 pixels. A subset size of 25 is selected according to the granularity of the speckle pattern. This means that the "edge" displacement data points entering

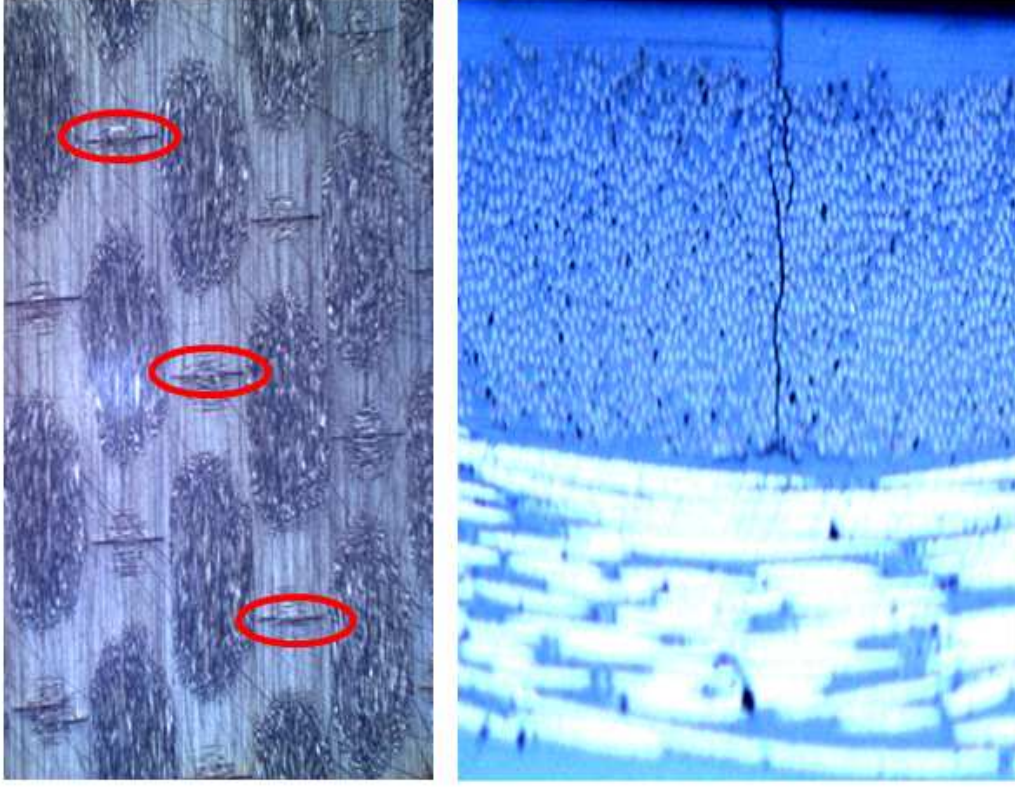


Fig. 10. Top surface of the specimen after uni-axial loading (left panel) and cross-section of the edge of the specimen close to the top surface (right panel).

the strain window will also receive information from 12 pixels outside the actual strain window. As such, the strain window influence width and height are reduced to 53 pixels. Since a step size of 5 pixels is adopted, Eq.(3) yields a maximum strain window of  $11 \times 11$  displacement data points.

In Figs.11-12 the maximum principal strain field  $\epsilon_1$  is displayed corresponding to a load of  $F = 35kN$ . We stress that at this load step no transverse cracking has occurred yet. The cracks appearing in Fig.10 are introduced at the end of the test at load values  $F > 40kN$ . As can be inferred, a nice strain pattern is reproduced, reflecting the produced diagonal strain pattern of the FE simulations and the visible cracks at the top surface. The uncorrected results, however, have an inherent gradient from the lower left to the upper right, which is physically not correct. The test is a uni-axial tensile test, so despite the local strain variations due to the local textile reinforcement architecture, the overall mean strain in axial direction should have the same value across the specimen, being the applied axial strain to the specimen. This gradient pattern is clearly removed by introducing lens distortion corrections in this 2D setup. The strain fields have an average magnitude of  $10000 \mu m/m$ . In view of the obtained strain accuracy of  $\approx 200 \mu m/m$  we can approach these results with confidence. To conclude, in this kind of experiments it is of the ut-



most importance to incorporate lens distortions in order to accurately describe high-strain gradients at the micro-strain level.

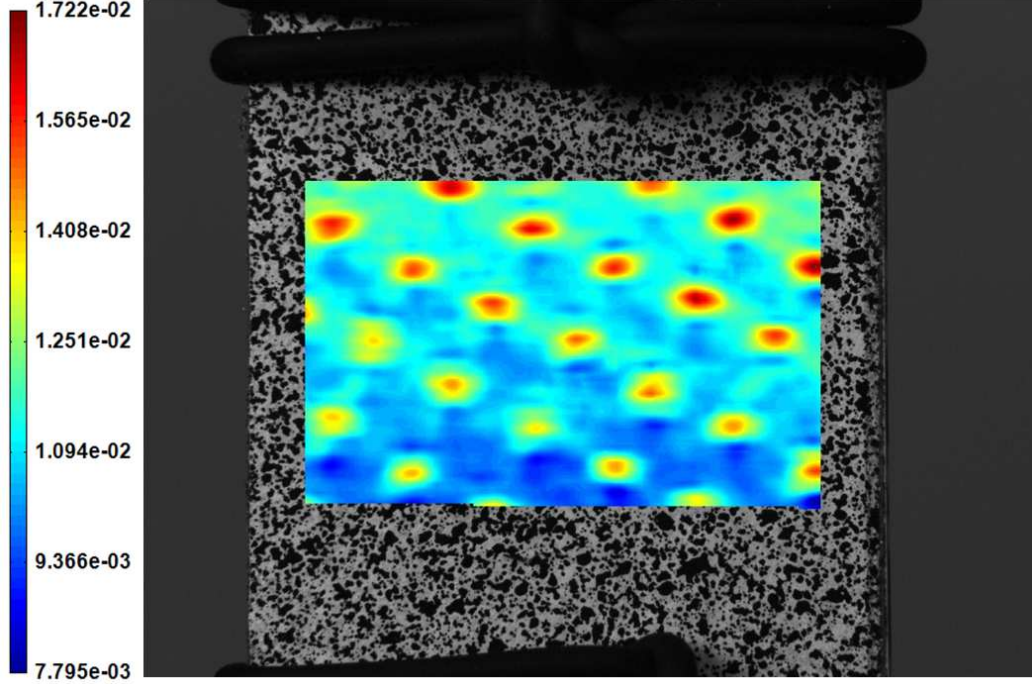


Fig. 11. Maximum principal strain component in  $m/m$  for a uni-axial tensile test on a fibre reinforced composite. Results are presented without the inclusion of lens distortion.

Finally, in order to investigate the evolution of the impact of lens distortions when proceeding from strains at the micro-strain level up to large values of plastic deformation, a uni-axial tensile test on steel SS304 is performed. Again, the camera is equipped with the Nikon 50 mm 1.4 lens and calibration parameters of the same order as listed in table 1 are obtained. Identical settings for the DIC algorithms are adopted: subset size  $25 \times 25$  pixels<sup>2</sup>, step size 5 pixels, strain window  $11 \times 11$  displacement data points, bicubic interpolation and an affine transformation order. The images are first processed without the inclusion of lens distortions yielding strain fields  $\epsilon_{uncorr}$ . Afterwards, the images are reprocessed incorporating corrections for lens distortions resulting in corrected strain fields  $\epsilon_{corr}$ . Accordingly, the mean and standard deviations of the relative differences  $\Delta(\epsilon)/\epsilon = (\epsilon_{uncorr} - \epsilon_{corr})/\epsilon_{uncorr}$  can be calculated. The results of this are summarized in Fig.13. As can be inferred, the impact of lens distortions is substantial at the micro-strain level showing large deviations between the corrected and uncorrected strain fields. At higher strain values ( $\geq 0.02m/m$ ) their influence largely cancels and corrections for lens distortions are of minor importance for the derived strain fields. This is not surprising in view of the larger signal to noise ratio when probing higher values of plastic deformation. It is important to note, however, that the lower limit of  $0.02 m/m$  is only approximate and only valid for this specific experimental

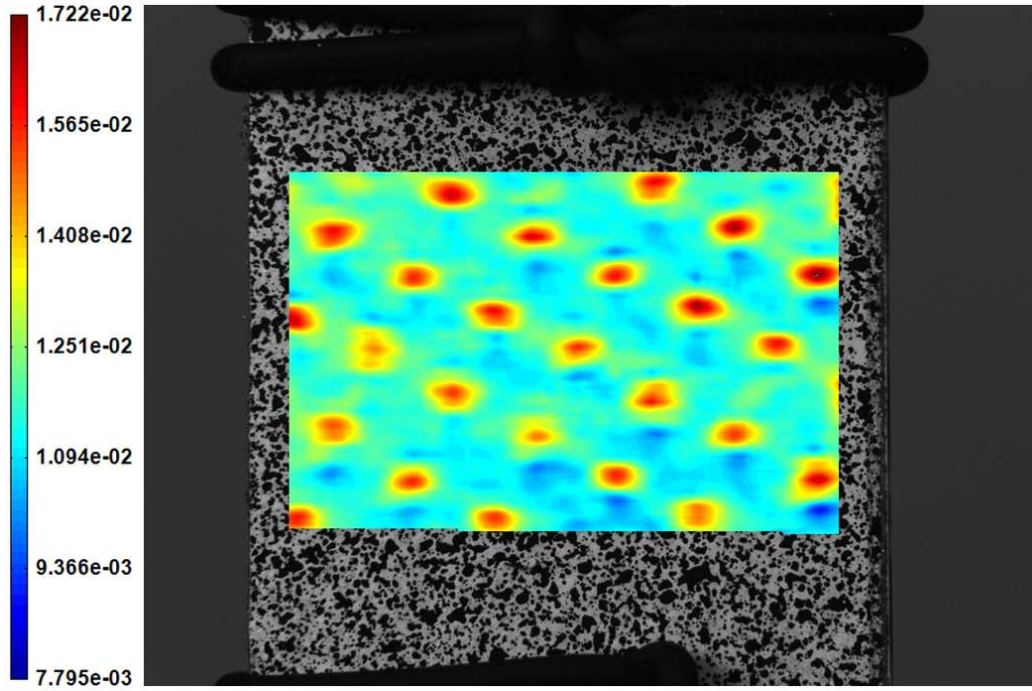


Fig. 12. Same as in Fig.11 but with lens distortion corrections.

setup. Other camera and lens combinations could lead towards lower or higher threshold values.

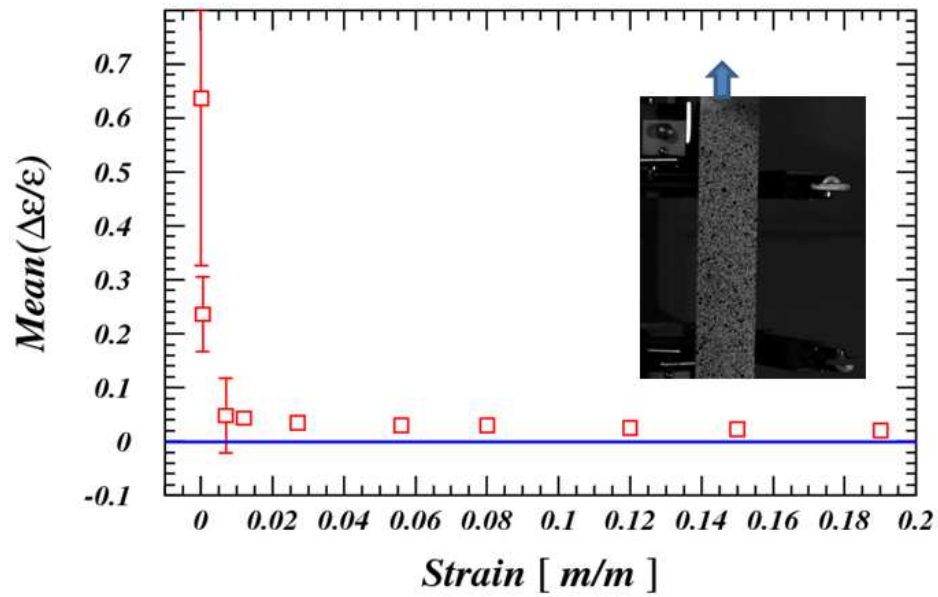


Fig. 13. Impact of lens distortions at low and high values of strain.

## 5 Conclusions

We investigated the impact of lens distortions on the accuracy of strain field measurements in both single and stereo camera experiments. In order to quantify the accuracy of DIC in strain measurements at the micro-strain level we performed rigid body motion experiments. It is shown that the impact of distortion corrections is substantial, improving the accuracy up to 200 micro-strain in a very basic DIC setup. Next, a uni-axial tensile test on a fibre reinforced composite material is performed inducing high strain gradients at the micro-strain level. A much better description of the deformations involved is obtained when distortion corrections are introduced. Accordingly we recommend to perform a camera calibration and an appropriate lens distortion compensation in single camera experiments focussing on in-plane deformation measurements at the micro-strain level.

## References

- [1] Coppieters S, Cooreman S, Sol H, Van Houtte P and Debruyne D. J Mater Process Technol 2011;211:545-52.
- [2] Van Paepegem W, Shulev A, Roussev I, De Pauw S, Degrieck J and Sainov V. Opt Lasers Eng 2009;47:390-7.
- [3] Rossi M and Pierron F. Int J Solids Struct 2012;49:420-35.
- [4] Zhang R, He L. Opt Lasers Eng 2012;50:1001-7.
- [5] Bing P, Wu D, Xia Y. Opt Lasers Eng 2012;50:586-92.
- [6] Shi H, Ji H, Yang G, He X. Opt Lasers Eng 2013;51:47-53.
- [7] Daggumati S, Voet E, Van Paepegem W, Degrieck J, Xu J, Lomov S and Verpoest I. Compos Sci Technol 2011;71:1171-9.
- [8] Rajan V, Rossol M and Zok F. Exp Mech 2012;doi 10.1007/s11340-012-9617-1.
- [9] Lava P, Cooreman S, Coppieters S, De Strycker M and Debruyne D. Opt Lasers Eng 2009;47:747-53.
- [10] Lava P, Cooreman S and Debruyne D. Opt Lasers Eng 2010;48:457-68.
- [11] Wang Y, Sutton M, Bruck H and Schreier H. Strain 2009;45:160-78.
- [12] Haddadi H and Belhabib S. Opt Lasers Eng 2008;46:185-96.
- [13] Bornert M, et. al. Exp Mech 2009;49:353-70.
- [14] Sutton M, Yan J, Tiwali V, Schreier H and Orteu J. Opt Lasers Eng 2008;46:746-57.
- [15] Yoneyama S, Kitagawa A, Kitamura K and Kikuta H. JSME Int J Series A-Solid Mechanics and Mat Eng 2006;49:458-66.
- [16] Schreier H, Garcia D and Sutton M. Exp Mech 2004;44:278-88.
- [17] Zhang D, Luo M and Arolo D. Opt Eng 2006;45:033605.
- [18] MatchID, Web site: <http://www.matchid.org> [accessed on 13 August 2012].
- [19] Hartley R and Sturm P. Comput Vision Image Understanding 1997;68:146-57.
- [20] Abaqus, Theory Manual, Version 6.7, 2007 (Dassault Systemes).
- [21] Sutton M, Orteu J and Schreier H. 2009 *Image correlation for shape, motion and deformation measurements*(New York: Springer).
- [22] Triggs B, Mclauchlan P, Hartley R and Fitzgibbon A. 2000 *Bundle adjustment-a modern synthesis* (Berlin: Springer).
- [23] Tsai R. IEEE Int J Robot Automat 1987;RA-3:323-44.

- [24] Zhang Z. IEEE T Pattern Anal 2000;22:1330-4.
- [25] Hartley R and Zisserman A. 2000 *Multiple view geometry in computer vision* (UK:Cambridge University Press).
- [26] Salvi J, Armangue X and Battle J. Pattern Recogn 2002;35:1617-35.
- [27] Lucchese L. Image Vision Comput 2005;23:517-39.
- [28] Wang J, Shi F, Zhang J and Liu Y. Pattern Recogn. 2008;41:607-15.
- [29] Daggumati S, Van Paepegem W, Degrieck J, Praet T, Verhegghe B, Xu J, Ivanov D, Lomov S and Verpoest I. Compos Sci Technol 2011;71:1217-24.
- [30] Daggumati S, Van Paepegem W, Degrieck J, Xu J, Lomov S and Verpoest I. Compos Sci Technol 2010;70:1926-33.
- [31] Daggumati S, Van Paepegem W, Degrieck J, Xu J, Lomov S and Verpoest I. Compos Sci Technol 2010;70:1934-41.